Improvement of structural and electrochemical properties of NMC layered cathode material by combined doping and coating

Hamideh Darjazi , S. Javad Rezvani , Sergio Brutti , Francesco Nobili

PII: S0013-4686(21)01861-2
DOI: https://doi.org/10.1016/j.electacta.2021.139577
Reference: EA 139577

To appear in: *Electrochimica Acta*

Received date: 15 June 2021
Revised date: 15 October 2021
Accepted date: 10 November 2021

Please cite this article as: Hamideh Darjazi , S. Javad Rezvani , Sergio Brutti , Francesco Nobili , Improvement of structural and electrochemical properties of NMC layered cathode material by combined doping and coating, *Electrochimica Acta* (2021), doi: https://doi.org/10.1016/j.electacta.2021.139577

Highlights

- Pristine and modified (by doping and coating) NMC(333) cathode materials are synthesized.
- Physico-chemical characterization reveals improved structural and morphological properties for the modified material.
- Electrochemical characterization reveals more stable cycling behavior for the modified cathode.
- Electrochemical impedance spectroscopy shows suppression of phase transition and more stable interfacial properties for the modified cathode.

Improvement of structural and electrochemical properties of NMC layered cathode material by combined doping and coating

Hamideh Darjazi[a], S. Javad Rezvani[b,c], Sergio Brutti[d,e], Francesco Nobili[a,e,]*

[a]*School of Science and Technology, Chemistry Division, University of Camerino, Via S. Agostino 1, 62032 Camerino (MC), Italy.*

[b]*School of Science and Technology, Physics Division, University of Camerino, Via Madonna delle Carceri 9B, 62032 Camerino (MC), Italy.*

[c]*Consiglio Nazionale delle Ricerche (CNR), IOM-CNR, Laboratorio TASC, Basovizza SS-14, km 163.5, 34149 Trieste, Italy.*

[d]*Dipartimento di Chimica, Università di Roma La Sapienza, P.le A. Moro 5, 00185 Roma, Italy.*

[e]*GISEL—Centro di Riferimento Nazionale per i Sistemi di Accumulo Elettrochimico di Energia, INSTM, via G. Giusti 9, 50121 Firenze, Italy.*

* Corresponding author: francesco.nobili@unicam.it; Tel: +39-0737-402216

Abstract

Prospective cathode materials, pristine and Mg-/Zr-modified $LiNi_{0.33}Mn_{0.33}Co_{0.33}O_2$ (NMC333), are successfully synthesized through a synthetic method including a citric acid-assisted sol-gel processing followed by drying and calcination at different temperatures. The combined results from structural, chemical, and morphological investigations reveal that the modified NMC, where the modification is obtained by doping and a uniform coating layer with an optimal thickness, show a better-organized layered structure and improved interfacial properties compared to the pristine NMC. The modified NMC material shows a remarkable improvement in terms of capacity retention, especially when setting the charge cut-off voltage at 4.2 V, which results in improved cycling stability after more than 200 cycles with capacity retention of around 95%. In order to shed light on the kinetics of redox processes, and its impact on charge/discharge behavior, electrochemical impedance spectroscopy is carried out at different states of charge during oxidation and reduction for both pristine and modified NMC-based electrodes. The

promising results obtained with this synthesis open possibilities for performance improvements of intercalating layered oxides by structure doping and surface enhancement.

Keywords: Li-ion batteries; cathode materials; $LiNi_{1/3}Co_{1/3}Mn_{1/3}O_2$ (NMC); doping/coating; sol-gel synthesis.

1. Introduction

Rechargeable lithium-ion batteries are widely used in portable electronics, power tools, electrified vehicles (hybrid, plug-in hybrid and fully electric), due to the unmatchable combination of high energy density and power density [1]. The current research on Li-ion batteries responds to the demand for advanced materials capable of reducing overall costs and environmental impacts, as well as providing higher energy density, lighter weight and better electrochemical properties [2]. Currently, $LiCoO_2$ is the most commercially used intercalation-type cathode material for Li-ion batteries, due to its high operating voltage, high theoretical specific capacity, good cycling performance and ease of preparation [1,3,4]. However, the cost of cobalt and the toxicity of the material, in addition to the poor thermal stability, push to develop positive electrodes with possible alternative materials [1,5,6]. Current efforts in the area, focused on the improvement of cathode materials, resulted in the formulation of the ternary oxides $LiNi_aCo_bMn_cO_2$ (where a + b + c =1), also called NMC. NMC materials have drawn significant attention as promising positive electrode materials in lithium ion batteries to offer an increased energy density [7].

Nowadays, among different types of NMC materials ($LiNi_{0.33}Mn_{0.33}Co_{0.33}O_2$ (NMC333), $LiNi_{0.5}Mn_{0.3}Co_{0.2}O_2$ (NMC532), $LiNi_{0.6}Mn_{0.2}Co_{0.2}O_2$ (NMC622), $LiNi_{0.8}Mn_{0.1}Co_{0.1}O_2$ (NMC811), etc.), NMC333 is as a well-investigated cathode, considering the low cost, good thermal stability and capability of inserting a significant amount of lithium in the transition metal sites, resulting in relatively high specific capacity [8]. Consequently, it is increasingly used in the battery market [1].

Detailed characterizations of the electronic structure of NMC materials with different Ni:Mn:Co contents revealed that the alteration of Ni^{2+}/Ni^{3+} and Co^{2+}/Co^{3+} ratios changes structural stability, electrical conductivity, thermal stability, and lattice parameters in different NMC compositions [9]. As a consequence, the most stable structure appears to be the NMC333, where Mn, Ni and Co mostly exhibit as Mn^{4+}, Ni^{2+}, and Co^{3+} states (inactive Jahn-Teller cations). To further stabilize the cathode structure, and enhance its electron conduction properties, two of the most effective approaches are lattice doping and surface coating [10]. Different doping and surface coatings have been studied to enhance the electrochemical performances of NMC [11–14]. However, the doping approach may give rise to the presence of an impurity phase, increased mixed cation, and distorted crystal structure [8]. Besides, surface modification with a uniform coating layer with an ideal thickness continues to be a challenge for the development of NMC cathode materials. Therefore, researchers still have to put considerable efforts to improve the electrochemical performance of NMC cathode materials. In this study we introduce mixed doping of NMC333 by both Zr^{4+} (r = 0.79Å), which is considered as a good candidate to increase the structural stability by decreasing the degree of Li^{+}/Ni^{2+} cation mixing [10], and Mg^{2+}, which has an ionic radius of r = 0.66Å similar to Ni^{2+} (r = 0.69Å) [15–17]. By introducing excess cations with respect to Li^{+} in the synthesis (meaning that the ratio (Ni+Mn+Co+dopants):Li is higher than 1), the doping may be expected to yield composite materials, where the doped active material is mixed with additional metal oxide phases, possibly coating or decorating the active material grains. This behavior has been previously demonstrated with the doping of the parent compound $LiCoO_2$ by excess amounts of aliovalent Zr^{4+} and Mg^{2+}, resulting in the formation of a composite $LiCo_{0.94}Zr_{0.06}O_2$ /MgO/ZrO_2 [18].

The morphological structure, crystallinity, particle size, and electrochemical performance of NMC cathode materials directly depend on the synthesis method. A multitude of routes has been

pursued to synthesize NMC cathode materials, namely hydrothermal method [19], combustion method [20], co-precipitation [21], solid-phase method [22], sol-gel method [4], etc. In this context, the present work deals with the synthesis of pristine NMC(333) (labeled as p-NMC) and Mg/Zr-modified NMC(333) (labeled as m-NMC) materials through a sol-gel method. The advantages of this synthesis route include easy upscaling, low cost, control of the stoichiometric ratio of the raw material components, and the possibility of homogeneous mixing [8,23]. The electrochemical investigations of p-NMC and m-NMC demonstrate that modification by Mg and Zr results in enhanced stability of the active phase and improved Li^+ and e^- transfer kinetics. Besides, particular attention is paid to the cycling potential window, in order to investigate possible enhancements of charge/discharge performance and stability. Finally, direct observation are made on interfacial and transport properties by electrochemical impedance spectroscopy, both on p-NMC and m-NMC, in order to relate structural properties, bulk conductivity, and cycling behavior.

2. Experimental Section

2.1. Material synthesis

The present research proposes a simplified method to prepare $LiNi_xCo_yMn_zO_2$ cathode materials involving sol-gel technique. The process is a modification of the synthesis successfully applied for the modification of the parent compound $LiCoO_2$ [18]. p-NMC was synthesized by dissolving stoichiometric amounts of lithium nitrate [$LiNO_3$], nickel (II) nitrate hexahydrate [$Ni(NO_3)_2{\cdot}6H_2O$], cobalt (II) nitrate hexahydrate [$Co(NO_3)_2{\cdot}6H_2O$], and manganese nitrate hexahydrate [$Mn(NO_3)_2{\cdot}4H_2O$] in ethylene

glycol. Then, a stoichiometric amount of citric acid (citric acid:(Ni+Mn+Co) 1:1) was added to the solution and stirred continuously at 70 °C for 1 hour (all chemicals from Sigma-Aldrich). The whole solution was evaporated by increasing temperature slowly to 200 °C while stirring for about 5 hours until a xerogel was obtained. The resulting material was ground with a mortar and pestle. The thermal treatment conditions commonly play a critical role on electrochemical performance of layered cathode materials [24]. In the present study, the same conditions successfully adopted for the parent $LiCoO_2$, were applied, corresponding to heat treatment at 250 °C for 24h after a heating ramp at a rate of 2 °C/min to decompose organic constituents [4], and further calcination at 750 °C for 24h after a heating ramp at a rate of 3.7 °C/min. The same complex sol–gel technique has been applied to the preparation of m-NMC by adding 5% of each magnesium nitrate hexahydrate [$Mg(NO_3)_2 \cdot 6H_2O$] and zirconium (IV) acetate hydroxide [$Zr(OH)_n \cdot (CH_3COO)$] to the ethylene glycol solution of the Ni, Mn, Co precursors, modifying the stoichiometric ratio of the cations as described by "$LiNi_{0.33}Co_{0.28}Mn_{0.33}Mg_{0.05}Zr_{0.05}O_2$" (characterization of the exact phase composition is given in Section 3.1).

2.2. Material characterization

The crystalline phases of materials were estimated by X-ray diffraction (XRD) using a Philips diffractometer equipped with Cu-K_α radiation (λ= 1.54059 Å) and Bragg-Brentano geometry in the 2θ range of 10°-70°. The morphology of the samples has been recorded by field emission Scanning Electron Microscopy (a FESEM Cambridge Stereo scan 360 electron microscope) and Transmission Electron Microscopy (TEM, FEI Tecnai

200 kV cryo-TEM instrument). TEM pictures have been analyzed using the ImageJ software [25]. In particular radial integration of the diffraction patterns has been calculated, after calibration, on a selected round area of the electron diffraction pattern using the routines embedded in the code.

X-ray Photoemission Spectroscopy (XPS) measurements were carried out via an in-house XPS apparatus. The powders were shaped into pellets and were introduced via a specially designed load lock chamber into the measurement chamber. The measurements were carried out using a focused Al K radiation (hν = 1486.6 eV) with the base chamber pressure of 10^{-9} mbar. Distinct points on each sample were scanned with a short dwell time to confirm the homogeneity of the sample as well as radiation degradation prevention. Core peaks were analyzed using a nonlinear Shirley background. The elemental concentrations were determined using Inductively Coupled Plasma (ICP-MS) Agilent Technologies, 7500 cx series, after dissolution by HCl and HNO_3.

2.3. Electrode preparation and electrochemical characterization

For the electrode preparation, a solution of Polyvinylidene fluoride (PVDF) in N-methylpyrrolidone (NMP) (both chemicals from Sigma-Aldrich) was prepared and stirred. The mixture of active materials and conductive carbon Super C65 (Timcal) was obtained by mixing and grinding. Thereafter, this mixture was subsequently added to the PVDF/NMP solution, resulting in a slurry with an active material:Super C65:PVDF composition equal to 80:10:10 (mass ratio). The process of stirring was continued for 6 h until a homogenous slurry was obtained. Then, the slurries were doctor-bladed (150 µm

gap) onto aluminum foil. The layers were heated at 70 °C for 2 h and then dried at room temperature. The layers were pressed and cut (the thickness of the cathode films was about 50 µm). Finally, the electrodes were dried under vacuum overnight at 120 °C. The electrodes were brought into a glove box (Jacomex, water, and oxygen contents below 0.9 ppm) to assemble T-shape polypropylene Swagelok-type 3-electrode cells, by using Li metal (Sigma-Aldrich) as reference and counter electrodes. A glass fiber (Whatman GF/A) was used as a separator and a solution of 1 M $LiPF_6$ in ethylene caronate:dimethyl carbonate (EC:DMC) 1:1 v/v (pre-formulated by Solvionic, France) was used as an electrolyte. The cell was sealed and removed from the glovebox for electrochemical testing.

Cyclic voltammetry (CV) and galvanostatic charge/discharge cycles were performed using a VMP-3Z multi-channel electrochemical workstation by Bio-Logic (France). All the cells were kept 12 h at open circuit voltage (OCV) before running all the electrochemical measurements. Cyclic voltammetry was run at a scanning rate of 0.05 mV/s in the voltage range between 3 and 4.5 V. Galvanostatic charge-discharge cycles of the cells were performed at 280 mA g^{-1} current, calculated with respect to active material mass. Electrochemical impedance spectroscopy (EIS) measurements were acquired using 3-electrode EL-CELL ECC-Ref cell assembly in the frequency range 15 mHz to 100 kHz. The bias potential values were scanned by potentiostatic steps of 25 mV (equilibration time of 1 h each) during the first two Li-extraction/insertion cycles. All the measurements have been run at T = 25°C. All potential values are given vs. Li^+/Li couple.

3. Results and discussion

3.1. Structural investigations

The compositions of both pristine and modified NMC materials were determined by ICP studies. The mass concentration ratio was found to be close to the expected compositions and confirmed the presence of Zr and Mg (ICP results are shown in table S1).

The phase and structure of p-NMC and m-NMC powders were investigated by X-ray diffraction (XRD). Fig. 1a shows the XRD patterns of both synthesized cathode materials. Their crystal structure is consistent with that of NMC materials and can be described as a layered oxide structure based on a hexagonal α-$NaFeO_2$ with space group R-3m [26] (no impurity phase has been detected). This suggests that the introduction of Mg and Zr does not change the layered ordering of the NMC structure. The primary reflections of the powders can be attributed to the strong [003] peak at 2θ around 18.6°. In addition, the distinct doublet-peak splits of the ([012]/[006]) and ([018]/[110]) at 2θ around 37° and 65° are visible, corresponding to well-ordered crystalline structures of NMC [27].

< Figure 1 here >

To ensure a reliable evaluation of the effect of doping on the structure of material, and to estimate the actual lattice parameters, Rietveld refinement analysis of the data was performed. The calculated parameters are presented in Table 1 (the comparison between the experimental and the simulated profiles is shown in Fig. 1b,c).

Table1: Rietveld refinement results for p-NMC and m-NMC materials.

Sample	Lattice parameter *a* /Å	Lattice parameter *c* /Å	c/a	$I_{(003)}/I_{(104)}$	$d_{(003)}$/Å	R_W (%)	R_P (%)
p-NMC	2.8587	14.2242	4.9757	1.45	4.7544	3.12	3.57
m-NMC	2.8691	14.2459	4.9652	1.53	4.7621	3.11	3.61

The cell parameters *a* and *c*, as well as the corresponding cell volume of the m-NMC material, are higher than for p-NMC. This suggests the effectiveness of the doping, resulting in an expansion in both directions of the [MO_2] layers. When the size of both dopants and "pristine" cations is taken into account, it results that the ionic radius of Mg^{2+} (0.66 Å) is quite similar to that of Ni^{2+} (0.69 Å), while larger than those of Co^{3+} (0.545 Å) and Mn^{4+} (0.53 Å). On the other side, the ionic radius of Zr^{4+} (0.79 Å) is much larger [9,10]. This suggests that the cell expansion is mostly due to Zr^{4+} doping into the structure [10], while doping by Mg^{2+} and formation of different oxide phases, such as MgO or ZrO_2, decorating the active material surface cannot be excluded. The calculated *c*/*a* ratio, higher than 4.9, confirms a well-ordered hexagonal structure. The I(003)/I(104) value is over 1.2 for both samples, which is evidence of small cation mixing (for m-NMC is slightly higher, therefore lower capacity decay and better cycling behaviors are to be expected for m-NMC [5], as well as a faster diffusion of Li^+ between [MO_2] layers because of the larger unit cell volume).

The electrochemical properties of active materials strongly depend on morphological properties, such as the size distribution of particles [4]. Therefore, the morphology was analyzed using SEM and TEM. Fig. 2a,e shows SEM images of p-NMC and m-NMC. Noticeable differences between the two samples can be observed. The p-NMC displays

an irregular polyhedron-like shape with a particle size approximately in the range of 80-250 nm. The smaller particles also exhibit relevant agglomeration into larger aggregates. On the contrary, m-NMC exhibits a much smaller particle size, homogeneously distributed around 35 nm. No aggregation is evidenced. The smaller particle size commonly accounts for easier insertion and deinsertion of Li^+ ion, by enlarging the active material/electrolyte interfacial area and reducing the solid-state ion diffusion pathways during charge and discharge processes [4],[28]. Thus, these results suggest that superior electrochemical activities may be expected for m-NMC.

TEM images in Fig. 2b,f confirm that the size of the m-NMC particles is about one order of magnitude lower than p-NMC. Further magnification (Fig. 2c,g) reveals that both materials are well crystallized, as already suggested by the very narrow XRD peaks shape. However, m-NMC exhibits surface fringes without any evident regular arrangement. This suggests the presence of an amorphous coating layer surrounding the surface of the active material grains, with a width of 1-2 nm. The coating also appears to be very uniform and homogeneous, without any cracking or fissure. This result confirms our hypothesis that the Mg^{2+}/Zr^{4+} modification of NMC structure can lead to the presence of minor amounts of extra phases, here evidenced as a surface coating, in the m-NMC material. As a result, aggregation of the active material grains is inhibited, as confirmed here by the smaller particle size of m-NMC with respect to p-NMC. In addition, the coating layer may suppress the direct interaction of the active electrode material with HF traces in the electrolyte, thus enabling improved electrochemical performance [8, 27]. Phase analysis of active materials and coating has been performed by analyzing the electron diffraction patterns acquired by TEM. The ED ring patterns were indexed to a hexagonal lattice, like the NMC one (Fig. 2d,h,i,j). The ED patterns of both cells are quite

similar, however, few differences can be noticed. In particular, due to the much larger crystallite diameters of the p-NMC sample, its ED is typical of few close-packed single crystals whereas that of the m-NMC one is closer to a polycrystalline pattern. Remarkably, the estimates of the lattice parameters obtained by ED are in excellent agreement with those obtained by XRD (Table 1), confirming a slight expansion of the lattice induced by doping.

< Figure 2 here >

X-ray Photoemission Spectroscopy (XPS) measurements have been carried out on Mn, Co, Ni, Mg, Zr, and O edges, as shown in Fig. 3. For both p-NMC and m-NMC, Ni spectra show presence of Ni^{2+} and Ni^{3+}, while in the case of Mn the observed components can be attributed to Mn^{4+} and Mn^{3+}. Co spectra clearly show a broadening and oxidation to a higher valence state in the modified sample. The m-NMC shows a relatively strong Mg^{2+} signal which confirms the presence of MgO at the surface. However, on the surface, the modified sample does not show a signal from Zr due to the lower cross-section of Zr at the incident photon energy used. This excludes that Zr^{4+} is part of the coating and suggests that, on the contrary, it is incorporated as a doping cation in the bulk. The O 1s spectra of the samples show broad features for which the component identification is difficult, due to the coincidence of Mn-O, Ni-O, Co-O binding energies, all being in the range between 529-531 eV. However, the m-NMC shows a stronger contribution at higher binding energy, which can be attributed to Mg-O and Co-O components.

< Figure 3 here >

3.2. Elechtrochemical investigations

In order to probe the electrochemical processes taking place at p-NMC and m-NMC materials during charge and discharge, cyclic voltammetry (CV) experiments were carried out, as shown in Fig. 4. The CV curves of p-NMC and m-NMC electrodes, recorded during the initial cycle, indicate reversible redox activities. During the first scan, both electrodes display a peak due to the sequential $Ni^{2+}/Ni^{3+}/Ni^{4+}$ oxidation during charge and $Ni^{4+}/Ni^{3+}/Ni^{2+}$ reduction during discharge [29]. The second oxidation peak for pristine electrode at the potential of 4.25 V was assigned to structural re-arrangement upon cycling, which can be related to Ni charge compensation during Li ion insertion/extraction [30], [31]. First-oxidation irreversibility is commonly evidenced by $LiMO_2$-type cathodes in this potential region [32]. However, this peak is not evidenced by m-NMC, confirming the impact of modification toward the stabilization of the structure. The values of peak separation ΔE_p ($E_{oxidation}$ - $E_{reduction}$) of the pristine electrode and modified electrode approach 90.4 mV and 80.8 mV, respectively. The decreased peak separation, together with sharper peak shape, suggests lower polarization and faster intercalation/deintercalation kinetics of m-NMC [26].

< Figure 4 here >

In order to investigate the cycling performance and stability, electrodes based on p-NMC and m-NMC active materials were subject to galvanostatic cycling at 280 mA g^{-1} (corresponding to 2C rate when a practical capacity of 140 mAh g^{-1} is considered), in a potential range of 3 V ≤ E ≤ 4.5 V. The trends of discharge capacity upon cycling are reported in Fig. 5a, while the charge/discharge E vs. Q profiles are shown in Fig. 5b,c.

The charge/discharge profiles evidence that the initial discharge capacity of the p-NMC cathode at 2C in the voltage range between 3 V and 4.5 V is 159 mAh g^{-1}, which is slightly higher than that of m-NMC (141 mAh g^{-1}). The lower specific capacity of m-NMC cathode can be due to the presence of electronic-insulator and ionic-conductor properties of the MgO coating layer (confirmed by TEM and XPS results). However, upon cycling, the m-NMC-based cathode retains higher capacity than p-NMC.This behavior can be attributed to the combined doping and coating, which enhance the structural and interfacial stabilities, respectively. It is worth noting that the low amounts of doping cations allow maintaining the original layered crystal structure during diffusion of Li^+ ions. Mg^{2+} ions retain the divalent state during cycling, and occupy the Li sites, inhibiting any local collapse of the inter-slab space [17,33–35] due to Li^+/Ni^{2+} cation mixing (in contrast, too high amounts of Mg^{2+} could have hindered the Li^+ diffusion and strongly affected the cell performance, resulting into a rapid capacity loss [16,17]). Additionally, the introduction of pillar ions (Mg^{2+}) in Li slabs leads to offset electrostatic repulsion between adjacent oxygen layers through Mg^{2+}– O^{2-} electrostatic attraction, so slowing c axis changes and decreasing volume change and preventing the interslab collapse [36]. Doping Zr^{4+} stabilizes the bulk structure as well, also facilitating insertion/extraction of Li^+ and decreasing resistance for Li^+ diffusion because of unit cell expansion. At the same time, aliovalent doping appears to foster bulk electron conduction and facilitates reduction in particle-size, which can lead to better electrochemical properties. Finally, the MgO coating leads to improvement of the interfacial properties, resulting in a more stable charge/discharge behavior upon long-term cycling. All these factors concur in improving the electrochemical activity of the material and result in higher capacity retention [10]. This behavior is confirmed by the coulombic efficiency values of the two electrodes. In fact, the initial coulombic efficiency for p-NMC and m-

NMC is 70.5% and 71.5%, and for following cycles reach 98.6 % and 99.2%, respectively.

Reduced polarization for the m-NMC cathode with respect to the p-NMC one can be observed in Fig. 5b,c, where the charge/discharge voltage hysteresis appears to be reduced for the doped/coated cathode. A negligible decrease in first-cycle irreversible capacity for the modified cathode is evidenced as well.

The charge/discharge behavior of m-NMC cathode has also been investigated within a narrower potential window (3.2 V ≤ E ≤ 4.2 V), by performing galvanostatic cycles at the same specific current value (280 mA g^{-1}). It can be seen from Fig. 5d that the discharge capacity for the m-NMC cathode cycled between 3.2 V and 4.2 V is 123 $mAhg^{-1}$, with excellent cycling retention (100% after 100 cycles, 95% after 200 cycles). This behavior reflects a common trend where NMC(333) cathodes at lower charge cut-offs enable slightly lower specific capacities, but much better capacity retention. On the contrary, the faster capacity decay at 4.5 V cut-off can be correlated with a more pronounced active material degradation, which hinders the Li^+ ion intercalation/deintercalation activity [37]. Table S2 lists some literature data of electrochemical performances of modified NMC(333) cathodes [11,14,38–42]. It should be noted that, despite the much higher specific current here adopted, the performances shown in the present paper for m-NMC cathode are comparable or even higher than those reported for the literature modified NMC(333) materials cycled in comparable potential ranges.

In order to further evaluate the impact of the different cut-off voltages on the electrochemical behavior, the evolution of discharge plateaus upon cycling has been

monitored. The exact potential values of the plateaus at first and hundredth cycles have been calculated for the m-NMC cathode cycled in the two different voltage ranges by plotting d^2Q/dV^2, as suggested by Ruan and co-workers [37] (see Fig. S2). The corresponding Q vs. E discharge profiles and the calculated plateau values are reported in Fig. 5e,f. During the first cycle, the discharge voltage plateaus for p-NMC and m-NMC cells are 3.76 V and 3.65 V, respectively. However, the voltage plateau value (3.72 V) evidenced after 100th cycles during discharge by the cell cycled in the narrower potential window (3.2 V ≤ E ≤ 4.2 V) is higher than the value (3.55 V) obtained with the cell cycled in the larger window (3 V ≤ E ≤ 4.5 V), thus demonstrating the positive impact of the lower-potential cut-off toward the stable cycling behavior of the cathode.

< Figure 5 here >

In order to shed light on the kinetics of the charge/discharge processes and their reversibility, electrochemical impedance spectroscopy (EIS) analysis has been performed. The EIS measurements have been carried out by recording sequences of spectra, during the oxidation and reduction steps of the initial two cycles, at closely spaced bias potentials (steps of 25 mV) over the potential windows 3 to 4.5 V, at T = 25 °C, for both p-NMC and m-NMC cathodes. Selected Nyquist plots acquired for both cathodes are shown in Figs. 6,7 (for sake of brevity, only the impedance dispersions related to the first cycle are shown). All the plots evidence the common features of the layered oxide compounds previously reported [15,18,32,43,44]. Namely, when the cells are at the beginning of the charge, corresponding to the foot of CV deintercalation peak (Figs. 6a and 7a, 3.0 V ≤ E ≤ 3.6 V, almost fully lithiated p-NMC and m-NMC), a large arc in the lower-frequency region (marked as A in Fig. 6a) dominates the dispersions, while a

semicircle at higher frequencies (marked as B in the inset) is shown. When the potential is increased, during the early stages of Li^+ deintercalation, the diameter of the arc A starts to decrease, and the semicircle B becomes more relevant. As shown in Figs. 6b and 7b, the large semicircle A further contracts and tends to bend toward the real axis at higher potentials and lower Li contents ($3.60\ V \leq E \leq 3.80\ V$, corresponding to CV peak in Fig. 4). When the potential is further increased to the range of $3.87V \leq E \leq 4.20\ V$ (Figs. 6c and 7c), a shoulder in the highest-frequency region (marked as C inthe inset of Fig. 6c) reveals the presence of a third semicircle, partly overlapped but easily detectable upon data analysis. At the same time, the two semicircles A and B start to grow again. Above 4.20 V, the diameter of the arc A is increased continuously for p-NMC (Fig 6d), while it further contracts for m-NMC (Fig 7d).

Figs. 6e-h and 7e-h show the Nyquist plots recorded during the first reduction of p-NMC and m-NMC, respectively. When the potential is lowered, for both p-NMC and m-NMC cathodes the diameter of arc A is progressively increased (panels e, f, g), however, the increase is more marked and evidenced earlier (meaning at higher potentials) in the case of p-NMC. Finally, below 3.57 V, the dispersions for both electrodes are dominated again by the low-frequency arc A (Figs. 6h and 7h).

To clarify these behaviors, the data related to first and second charge/discharge cycles have been fitted with RelaxIS software (rhd instruments, Germany) by using the equivalent circuit schematized as $R_{sol}(R_{sei}C_{sei})(R_{ct}C_{dl})([R_{elec}W]C_{elec})C_i$ in Boukamp's notation [45] and detailed in Fig. S2, where: (i) R_{sol} represents the Li^+ ion resistance across the electrolyte at the highest frequency intercept; (ii) $R_{sei,}$ and C_{sei} are related to the semicircle at high frequencies C and correspond to resistance and capacitance of the SEI layer, partly overlapped by (iii) R_{ct} and C_{dl}, which are related to semicircle B at middle frequencies and describe interfacial charge-transfer

resistance and double layer capacitance; (iv) R_{elec} and C_{elec} are assigned to the semicircle at low frequencies A and represent the electronic resistance and the capacitance of the accumulation of charge at the particles surface and/or at intraparticles crystallite domains; (v) W (Warburg diffusion element) and C_{int} (intercalation capacity), evidenced by the sloped line at the lowest-frequency limit, describe Li^+ ion diffusion to a blocking electrode [43]. In the fitting procedure, all the C elements have been substituted by constant-phase elements Q, in order to take into account any inhomogeneities or roughness of the electrodes [46].

< Figure 6 here >

< Figure 7 here >

Fig. 8a,b presents the overall trends of the calculated values of R_{sol}, R_{sei}, R_{ct}, and R_{elec} for p-NMC and m-NMC, respectively. For both electrodes, R_{elec} decreases during the oxidation down to 3.80 V (thus becoming a better electronic conductor [44]). Subsequently, from 3.80 to 4.20 V, an increase of R_{elec} can be detected, suggesting a partly irreversible structural rearrangement. This behavior is partly consistent with the results from Fröhlich et al. [30] and Shaju et al. [47]. These authors reported a reversible phase transition for NMC(333) materials occurring at around 3.8 V, with a behavior similar to Li $(Ni_{1/2}Mn_{1/2})O_2$ layered cathode materials, which undergo a phase transition from hexagonal (space group R-3m) for Li $(Ni_{1/2}Mn_{1/2})O_2$ to monoclinic (space group C2/m) for $Li_{0.5}(Ni_{1/2}Mn_{1/2})O_2$ [48].

However, in the potential range 4.20 to 4.50 V, two different behaviors can be observed. R_{elec} of p-NMC keeps increasing, evidencing that the phase transformation is still taking

place. This is consistent with a charge compensation mechanism, which involves $Ni^{2+/3+}$ [30],[31] and results in an increase of bulk material resistance. On the other side, the m-NMC cathode exhibits a further reduction of R_{elec} values, confirming that the phase transition is now hindered.

As regards the R_{elec} behavior during the subsequent reduction/oxidation scans, during the first-cycle reduction the R_{elec} values for both electrodes increase again of several order of magnitude, while through the second cycle the R_{elec} reversible contraction/expansion during oxidation/reduction are confirmed. These findings confirm that, while an irreversible strucutral rearrangement takes place during first charge, the cycle-upon-cycle insulator-to-conductor transition is mostly reversible.

As regards charge-transfer resistance, the calculated R_{ct} values of p-NMC exhibit a pronounced, continuous increase during the first oxidation and the initial steps of the subsequent reduction. However, for m-NMC the huge change is limited to the first oxidation, simultaneously with the partial rearrangement of the cell. Since R_{ct} changes are commonly related to rearrangements of the electrode/electrolyte interface and these are expected to occur as a consequence of phase rearrangements, the different R_{ct} behaviors make further evidence that the phase transition in m-NMC is more limited than in p-NMC. For both electrodes R_{ct} remains almost unchanged during the subsequent charge/discharge steps, confirming that no major structural and morphological rearrangements occur during the subsequent cycles.

Comparison of R_{elec} and R_{ct} values allows evaluating the rate-determining step of the reversible deintercalation/intercalation kinetics of p-NMC and m-NMC. At low

potentials, R_{elec} is much higher than R_{ct}, which confirms an insulator behavior of the electrode and limitations of redox kinetics by the bulk electronic conductivity of the oxide at higher Li contents [49]. At higher potentials, when the insulator-to-conductor transition is complete, R_{ct} becomes comparable with R_{elec}, suggesting that at lower Li contents the redox kinetics is controlled also by the rate of interfacial electron transfer between electrode and Li^+ ion. A similar trend has also been observed for Na-ion battery materials [50].

As regards the passivation layer, the calculated R_{sei} values exhibit a steady increase of about one order of magnitude through the two cycles for both electrodes, as a signature of the growth of interphase layer upon time. However, the m-NMC electrode reveals a more stable behavior, suggesting that the material modification is effective toward the interfacial stability as well. This is confirmed by the behavior of electrolyte resistance R_{sol}, which values increase at higher potentials during first oxidation for p-NMC, while they are almost constant for m-NMC. This confirms that the coating suppresses both the decomposition of electrolyte and the dissolution of active material due to HF traces in the electrolyte itself [29].

< Figure 8 here >

4. **Conclusions**

Although recent years have yielded the enhancement for the NMC cathode materials by modification, more effort is still needed to optimize NMC structural and interfacial stability. In this context, we have developed a facile approach for the synthesis of two NMC (333) materials,

pristine and modified by doping/coating, aimed at improving electrochemical performances of LIBs. The results showed a better-organized layered structure for the modified NMC, due to the doping and the homogenous coating with an optimal-thickness layer. Electrochemical tests revealed that capacity retention is improved by modification. In fact, the modified NMC presents an excellent cycling stability after more than 200 cycles without an obvious capacity fade at a charge cut-off voltage of 4.2 V. The evolution of the impedance spectra was shown for both p-NMC and m-NMC. According to EIS results, doping has considerable effect on electronic properties and structural stability, while the introduction of coating suppresses the electrolyte decomposition, leading to enhanced cycling performance.

In addition to demonstrating enhancement of NMC(333) cathode material stability and performance, the obtained results pave the way to facile methodologies for the improvement of structural and interfacial properties of the entire family of NMC cathodes.

Credit author statement

Conceptualization and methodology: F.N., H.D; Investigation: H.D., S.B., J.R.; Resources: F.N.; Writing – Original Draft: H.D.; Writing – review and editing: H.D., F.N.; Visualization: H.D., S.B., J.R.; Project Administration and Funding Acquisition: F.N.

Declaration of interests

☒ The authors declare that they have no known competing financial interests or personal relationships that could have appeared to influence the work reported in this paper.

References

[1] N. Nitta, F. Wu, J.T. Lee, G. Yushin, Li-ion battery materials: Present and future, Mater. Today. 18 (2015) 252–264. https://doi.org/10.1016/j.mattod.2014.10.040.

[2] S.B. Chikkannanavar, D.M. Bernardi, L. Liu, A review of blended cathode materials for use in Li-ion batteries, J. Power Sources. 248 (2014) 91–100. https://doi.org/10.1016/j.jpowsour.2013.09.052.

[3] P. Rozier, J.M. Tarascon, Review—Li-Rich Layered Oxide Cathodes for Next-Generation Li-Ion Batteries: Chances and Challenges, J. Electrochem. Soc. 162 (2015) A2490–A2499. https://doi.org/10.1149/2.0111514jes.

[4] R. Santhanam, B. Rambabu, Improved high rate cycling of Li-rich $Li_{1.10}Ni_{1/3}Co_{1/3}Mn_{1/3}O_2$ cathode for lithium batteries, Int. J. Electrochem. Sci. 4 (2009) 1770–1778.

[5] M.T. Tung, V.D. Luong, Synthesis , structural and electrochemical properties of Ni-rich material prepared by a sol-gel method, 54 (2016) 760–764. https://doi.org/10.15625/0866-7144.2016-00400.

[6] J.B. Goodenough, Y. Kim, Challenges for rechargeable Li batteries, Chem. Mater. 22 (2010) 587–603. https://doi.org/10.1021/cm901452z.

[7] C. Tian, F. Lin, M.M. Doeff, Electrochemical Characteristics of Layered Transition Metal Oxide Cathode Materials for Lithium Ion Batteries: Surface, Bulk Behavior, and Thermal

Properties, Acc. Chem. Res. 51 (2018) 89–96. https://doi.org/10.1021/acs.accounts.7b00520.

[8] L. Zhu, C. Bao, L. Xie, X. Yang, X. Cao, Review of synthesis and structural optimization of $LiNi_{1/3}Co_{1/3}Mn_{1/3}O_2$ cathode materials for lithium-ion batteries applications, J. Alloys Compd. 831 (2020) 154864. https://doi.org/10.1016/j.jallcom.2020.154864.

[9] H. Sun, K. Zhao, Electronic Structure and Comparative Properties of $LiNi_xMn_yCo_zO_2$ Cathode Materials , J. Phys. Chem. C. 121 (2017) 6002–6010. https://doi.org/10.1021/acs.jpcc.7b00810.

[10] S. Liu, Z. Dang, D. Liu, C. Zhang, T. Huang, A. Yu, Comparative studies of zirconium doping and coating on $LiNi_{0.6}Co_{0.2}Mn_{0.2}O_2$ cathode material at elevated temperatures, J. Power Sources. 396 (2018) 288–296. https://doi.org/10.1016/j.jpowsour.2018.06.052.

[11] K. Sahni, M. Ashuri, Q. He, R. Sahore, I.D. Bloom, Y. Liu, J.A. Kaduk, L.L. Shaw, H_3PO_4 treatment to enhance the electrochemical properties of $Li(Ni_{1/3}Co_{1/3}Mn_{1/3})O_2$ and $Li(Ni_{0.5}Mn_{0.3}Co_{0.2})O_2$ cathodes, Electrochim. Acta. 301 (2019) 8–22. https://doi.org/10.1016/j.electacta.2019.01.153.

[12] W. Cho, J.H. Song, K.W. Lee, M.W. Lee, H. Kim, J.S. Yu, Y.J. Kim, K.J. Kim, Improved particle hardness of Ti-doped $LiNi_{1/3}Co_{1/3}Mn_{1/3-x}Ti_xO_2$ as high-voltage cathode material for lithium-ion batteries, J. Phys. Chem. Solids. 123 (2018) 271–278. https://doi.org/10.1016/j.jpcs.2018.08.008.

[13] Z.C. Shao, J. Guo, Z. Zhao, J. Xia, M. Ma, Y. Zhang, Preparation and Properties of Al_2O 3-doping $LiNi_{1/3}Co_{1/3}Mn_{1/3}O_2$ Cathode Materials, Mater. Manuf. Process. 31 (2016) 1004–1008. https://doi.org/10.1080/10426914.2015.1117618.

[14] L. Yang, F. Ren, Q. Feng, G. Xu, X. Li, Y. Li, E. Zhao, J. Ma, S. Fan, Effect of Cu Doping on the Structural and Electrochemical Performance of $LiNi_{1/3}Co_{1/3}Mn_{1/3}O_2$ Cathode Materials, J. Electron. Mater. 47 (2018) 3996–4002. https://doi.org/10.1007/s11664-018-6284-8.

[15] F. Nobili, S. Dsoke, F. Croce, R. Marassi, An ac impedance spectroscopic study of Mg-doped $LiCoO_2$ at different temperatures: Electronic and ionic transport properties, Electrochim. Acta. 50 (2005) 2307–2313. https://doi.org/10.1016/j.electacta.2004.10.044.

[16] H. Zhang, Synthesis and characterization of $LiNi_{0.7\ x}Mg_xCo_{0.3}O_2$ ($0 \leq x \leq 0.1$) cathode materials for lithium-ion batteries prepared by a sol-gel method, Adv. Mater. Sci. Eng. 2014 (2014). https://doi.org/10.1155/2014/746341.

[17] R. Sathiyamoorthi, P. Shakkthivel, S. Ramalakshmi, Y.G. Shul, Influence of Mg doping on the performance of $LiNiO_2$ matrix ceramic nanoparticles in high-voltage lithium-ion cells, J. Power Sources. 171 (2007) 922–927. https://doi.org/10.1016/j.jpowsour.2007.06.023.

[18] F. Nobili, F. Croce, R. Tossici, I. Meschini, P. Reale, R. Marassi, Sol-gel synthesis and electrochemical characterization of Mg-/Zr-doped $LiCoO_2$ cathodes for Li-ion batteries, J. Power Sources. 197 (2012) 276–284. https://doi.org/10.1016/j.jpowsour.2011.09.053.

[19] L. Peng, Y. Zhu, U. Khakoo, D. Chen, G. Yu, Self-assembled $LiNi_{1/3}Co_{1/3}Mn_{1/3}O_2$ nanosheet cathodes with tunable rate capability, Nano Energy. 17 (2015) 36–42. https://doi.org/10.1016/j.nanoen.2015.07.031.

[20] P.K. Nayak, J. Grinblat, M. Levi, Y. Wu, B. Powell, D. Aurbach, TEM and Raman

spectroscopy evidence of layered to spinel phase transformation in layered $LiNi_{1/3}Co_{1/3}Mn_{1/3}O_2$ upon cycling to higher voltages, J. Electroanal. Chem. 733 (2014) 6–19. https://doi.org/10.1016/j.jelechem.2014.09.005.

[21] D. Peralta, J. Salomon, J.F. Colin, A. Boulineau, F. Fabre, C. Bourbon, B. Amestoy, E. Gutel, D. Bloch, S. Patoux, Submicronic $LiNi_{1/3}Co_{1/3}Mn_{1/3}O_2$ synthesized by co-precipitation for lithium ion batteries - Tailoring a classic process for enhanced energy and power density, J. Power Sources. 396 (2018) 527–532. https://doi.org/10.1016/j.jpowsour.2018.06.075.

[22] F. Xu, H. Yan, J. Chen, Z. Zhang, C. Fan, Ultrafine $LiNi_{1/3}Co_{1/3}Mn_{1/3}O_2$ powders via an enhanced thermal decomposition solid state reaction, J. Appl. Electrochem. 49 (2019) 647–656. https://doi.org/10.1007/s10800-019-01313-2.

[23] Z.D. Huang, X.M. Liu, S.W. Oh, B. Zhang, P.C. Ma, J.K. Kim, Microscopically porous, interconnected single crystal $LiNi_{1/3}Co_{1/3}Mn_{1/3}O_2$ cathode material for Lithium ion batteries, J. Mater. Chem. 21 (2011) 10777–10784. https://doi.org/10.1039/c1jm00059d.

[24] G. Sun, X. Yin, W. Yang, A. Song, C. Jia, W. Yang, Q. Du, Z. Ma, G. Shao, The effect of cation mixing controlled by thermal treatment duration on the electrochemical stability of lithium transition-metal oxides, Phys. Chem. Chem. Phys. 19 (2017) 29886–29894. https://doi.org/10.1039/c7cp05530g.

[25] M.D. Abràmoff, P.J. Magalhães, S.J. Ram, Image processing with imageJ, Biophotonics Int. 11 (2004) 36–41. https://doi.org/10.1201/9781420005615.ax4.

[26] J. Xu, S.L. Chou, Q.F. Gu, H.K. Liu, S.X. Dou, The effect of different binders on electrochemical properties of $LiNi_{1/3}Co_{1/3}Mn_{1/3}O_2$ cathode material in lithium ion batteries, J. Power Sources. 225 (2013) 172–178. https://doi.org/10.1016/j.jpowsour.2012.10.033.

[27] Z. Liu, Z. Zhang, Y. Liu, L. Li, S. Fu, Facile and scalable fabrication of K^+ -doped

$Li_{1.2}Ni_{0.2}Co_{0.08}Mn_{0.52}O_2$ cathode with ultra high capacity and enhanced cycling stability for lithium ion batteries, Solid State Ionics. 332 (2019) 47–54. https://doi.org/10.1016/j.ssi.2018.12.021.

[28] T. Aida, T. Toma, S. Kanada, A comparative study of particle size and hollowness of $LiNi_{1/3}Co_{1/3}Mn_{1/3}O_2$ cathode materials for high-power Li-ion batteries: effects on electrochemical performance, J. Solid State Electrochem. 24 (2020) 1415–1425. https://doi.org/10.1007/s10008-020-04640-z.

[29] Y. Xie, D. Gao, L.L. Zhang, J.J. Chen, S. Cheng, H.F. Xiang, CeF_3-modified $LiNi_{1/3}Co_{1/3}Mn_{1/3}O_2$ cathode material for high-voltage Li-ion batteries, Ceram. Int. 42 (2016) 14587–14594. https://doi.org/10.1016/j.ceramint.2016.06.074.

[30] K. Fröhlich, I. Abrahams, M. Jahn, Determining phase transitions of layered oxides via electrochemical and crystallographic analysis, Sci. Technol. Adv. Mater. 21 (2020) 653–660. https://doi.org/10.1080/14686996.2020.1814116.

[31] T. Li, X.-Z. Yuan, L. Zhang, D. Song, K. Shi, C. Bock, Degradation Mechanisms and Mitigation Strategies of Nickel-Rich NMC-Based Lithium-Ion Batteries, Springer Singapore, 2020. https://doi.org/10.1007/s41918-019-00053-3.

[32] F. Nobili, R. Tossici, F. Croce, B. Scrosati, R. Marassi, Electrochemical ac impedance study of $Li_xNi_{0.75}Co_{0.25}O_2$ intercalation electrode, J. Power Sources. 94 (2001) 238–241. https://doi.org/10.1016/S0378-7753(00)00592-9.

[33] C. Pouillerie, L. Croguennec, C. Delmas, $Li_xNi_{1-y}Mg_yO_2$ (y = 0.05, 0.10) system: Structural modifications observed upon cycling, Solid State Ionics. 132 (2000) 15–29. https://doi.org/10.1016/S0167-2738(00)00699-8.

[34] C. Pouillerie, F. Perton, P. Biensan, J.P. Pérès, M. Broussely, C. Delmas, Effect of magnesium substitution on the cycling behavior of lithium nickel cobalt oxide, J. Power Sources. 96 (2001) 293–302. https://doi.org/10.1016/S0378-7753(00)00653-4.

[35] Y. Cho, P. Oh, J. Cho, A new type of protective surface layer for high-capacity ni-based cathode materials: Nanoscaled surface pillaring layer, Nano Lett. 13 (2013) 1145–1152. https://doi.org/10.1021/nl304558t.

[36] H. Li, P. Zhou, F. Liu, H. Li, F. Cheng, J. Chen, Stabilizing nickel-rich layered oxide cathodes by magnesium doping for rechargeable lithium-ion batteries, Chem. Sci. 10 (2019) 1374–1379. https://doi.org/10.1039/c8sc03385d.

[37] Y. Ruan, X. Song, Y. Fu, C. Song, V. Battaglia, Structural evolution and capacity degradation mechanism of $LiNi_{0.6}Mn_{0.2}Co_{0.2}O_2$ cathode materials, J. Power Sources. 400 (2018) 539–548. https://doi.org/10.1016/j.jpowsour.2018.08.056.

[38] L. Zhu, L. Xie, C. Bao, X. Yan, X. Cao, $LiNi_{1/3}Co_{1/3}Mn_{1/3}O_2$/polypyrrole composites as cathode materials for high-performance lithium-ion batteries, Int. J. Energy Res. 44 (2020) 298–308. https://doi.org/10.1002/er.4916.

[39] S. Park, D. Kim, H. Ku, M. Jo, S. Kim, J. Song, J. Yu, K. Kwon, The effect of Fe as an impurity element for sustainable resynthesis of $Li[Ni_{1/3}Co_{1/3}Mn_{1/3}]O_2$ cathode material from spent lithium-ion batteries, Electrochim. Acta. 296 (2019) 814–822. https://doi.org/10.1016/j.electacta.2018.11.001.

[40] Y. Ma, P. Cui, D. Zhan, B. Gan, Y. Ma, Y. Liang, Enhancement of the electrochemical performance of $LiNi_{1/3}Co_{1/3}Mn_{1/3}O_2$ cathode material by double-layer coating with graphene oxide and SnO_2 for lithium-ion batteries, J. Nanomater. 2019 (2019). https://doi.org/10.1155/2019/7586790.

[41] J. Zhu, J. Yan, J. Chen, X. Guo, S. Zhao, Structuring Al^{3+}-doped $Li(Ni_{1/3}Co_{1/3}Mn_{1/3})O_2$ by 3D-birdnest-shaped MnO2, Funct. Mater. Lett. 12 (2019) 3–7. https://doi.org/10.1142/S1793604719500516.

[42] W. Liu, C. Li, X. Sun, X. Zhang, K. Wang, Z. Li, Q. Hao, Y. Ma, Improvement of the high-rate capability of $LiNi_{1/3}Co_{1/3}Mn_{1/3}O_2$ cathode by adding highly electroconductive

and mesoporous graphene, J. Alloys Compd. 758 (2018) 206–213. https://doi.org/10.1016/j.jallcom.2018.05.110.

[43] F. Nobili, R. Tossici, R. Marassi, F. Croce, B. Scrosati, An AC impedance spectroscopic study of Li_xCoO_2 at different temperatures, J. Phys. Chem. B. 106 (2002) 3909–3915. https://doi.org/10.1021/jp013569a.

[44] F. Croce, F. Nobili, A. Deptula, W. Lada, R. Tossici, A. D'Epifanio, B. Scrosati, R. Marassi, An electrochemical impedance spectroscopic study of the transport properties of $LiNi_{0.75}Co_{0.25}O_2$, Electrochem. Commun. 1 (1999) 605–608. https://doi.org/10.1016/S1388-2481(99)00123-X.

[45] B.A. Boukamp, A Nonlinear Least Squares Fit procedure for analysis of immittance data of electrochemical systems, Solid State Ionics. 20 (1986) 31–44. https://doi.org/10.1016/0167-2738(86)90031-7.

[46] J.R. Macdonald, a J. Wiley, Theory , Experiment , and, applications, second ed., John Wiley & Sons, New York, 2005, p. 83.

[47] K.M. Shaju, G. V. Subba Rao, B.V.R. Chowdari, Influence of Li-Ion Kinetics in the Cathodic Performance of Layered $Li(Ni_{1/3}Co_{1/3}Mn_{1/3})O_2$, J. Electrochem. Soc. 151 (2004) A1324. https://doi.org/10.1149/1.1775218.

[48] Y. Arachi, H. Kobayashi, S. Emura, Y. Nakata, M. Tanaka, T. Asai, Structural change of $Li_{1-x}Ni_{0.5}Mn_{0.5}O_2$ cathode materials for lithium-ion batteries by synchrotron radiation, Chem. Lett. 32 (2003) 60–61. https://doi.org/10.1246/cl.2003.60.

[49] F. Nobili, S. Dsoke, M. Minicucci, F. Croce, R. Marassi, Correlation of Ac-impedance and in situ X-ray spectra of $LiCoO_2$, J. Phys. Chem. B. 110 (2006) 11310–11313. https://doi.org/10.1021/jp0606356.

[50] M. Zarrabeitia, F. Nobili, M.Á. Muñoz-Márquez, T. Rojo, M. Casas-Cabanas, Direct observation of electronic conductivity transitions and solid electrolyte interphase stability

of $Na_2Ti_3O_7$ electrodes for Na-ion batteries, J. Power Sources. 330 (2016) 78–83. https://doi.org/10.1016/j.jpowsour.2016.08.112.

Figures Captions

Figure 1. XRD patterns of p-NMC and m-NMC powders (a); Rietveld refinement results of p-NMC (b), m-NMC (c).

Figure 2. SEM and TEM images of (a, b, c, d) p-NMC and (e, f, g, h) m-NMC samples. Indexed radial integration of the electron diffraction patterns from TEM for the p-NMC (i) and m-NMC (j) samples.

Figure 3. XPS spectra of p-NMC and m-NMC.

Figure 4. CV curves of p-NMC and m-NMC electrodes. Scan rate = 0.05 mVs^{-1}.

Figure 5. Charge/discharge capacity of p-NMC and m-NMC electrodes (a); charge/discharge profiles of selected cycles for p-NMC electrode (b), and m-NMC electrode (c). Charge/discharge capacity of m-NMC electrodes cycled in different potential windows (d); discharge profiles of 1^{st} and 100^{th} cycles for m-NMC electrode cycled in 3 V ≤ E ≤ 4.5 V range (e), for m-NMC electrode cycled in 3.2 V ≤ E ≤ 4.2 V range (c). I = 280 mA g^{-1}.

Figure 6. Nyquist plots recorded at selected potentials for p-NMC during the first oxidation (a-d) and during the first reduction (e-h).15 mHz < f < 100 kHz.

Figure 7. Nyquist plots recorded at selected potentials for m-NMC during the first oxidation (a-d) and during the first reduction (e-h).15 mHz < f < 100 kHz.

Figure 8. Fitted values of R_{sol}, R_{sei}, R_{ct}, R_{elec} during the first two cycles for (a) p-NMC and (b) m-NMC. 3 V ≤ E ≤ 4.5 V.

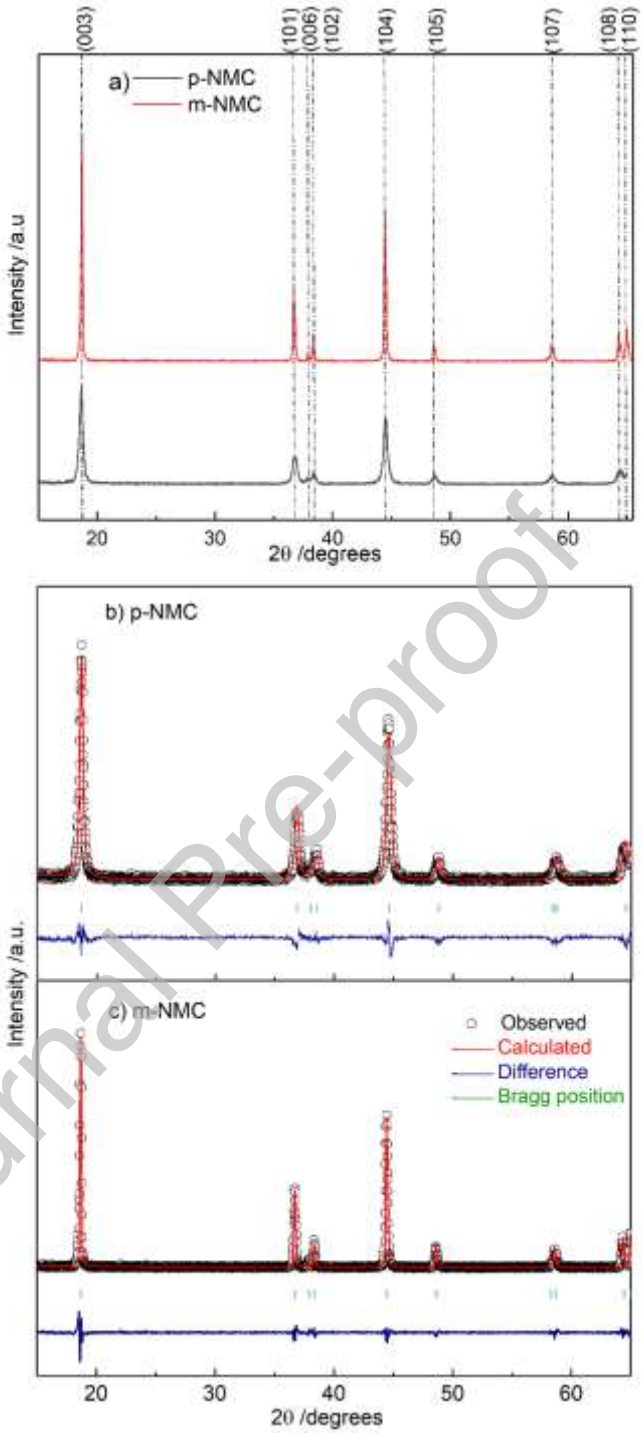

Figure 1. XRD patterns of p-NMC and m-NMC powders (a); Rietveld refinement results of p-NMC (b), m-NMC (c).

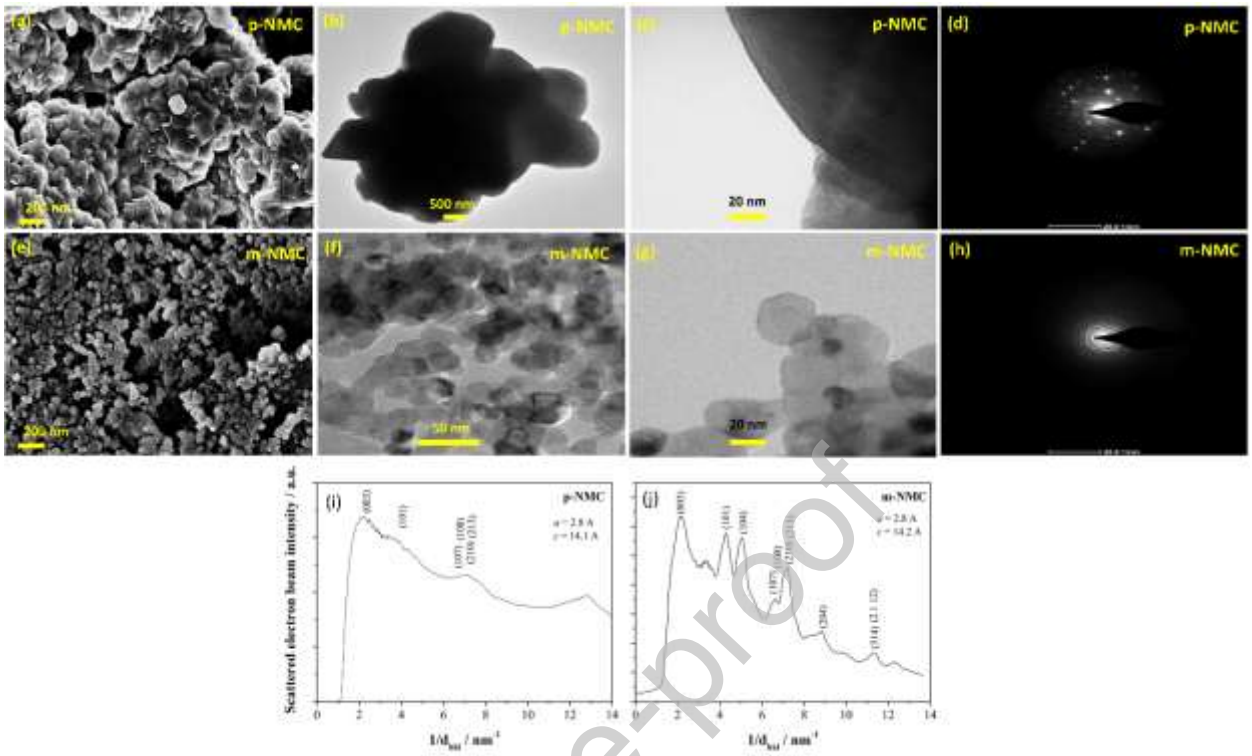

Figure 2. SEM and TEM images of (a, b, c, d) p-NMC and (e, f, g, h) m-NMC samples. Indexed radial integration of the electron diffraction patterns from TEM for the p-NMC (i) and m-NMC (j) samples.

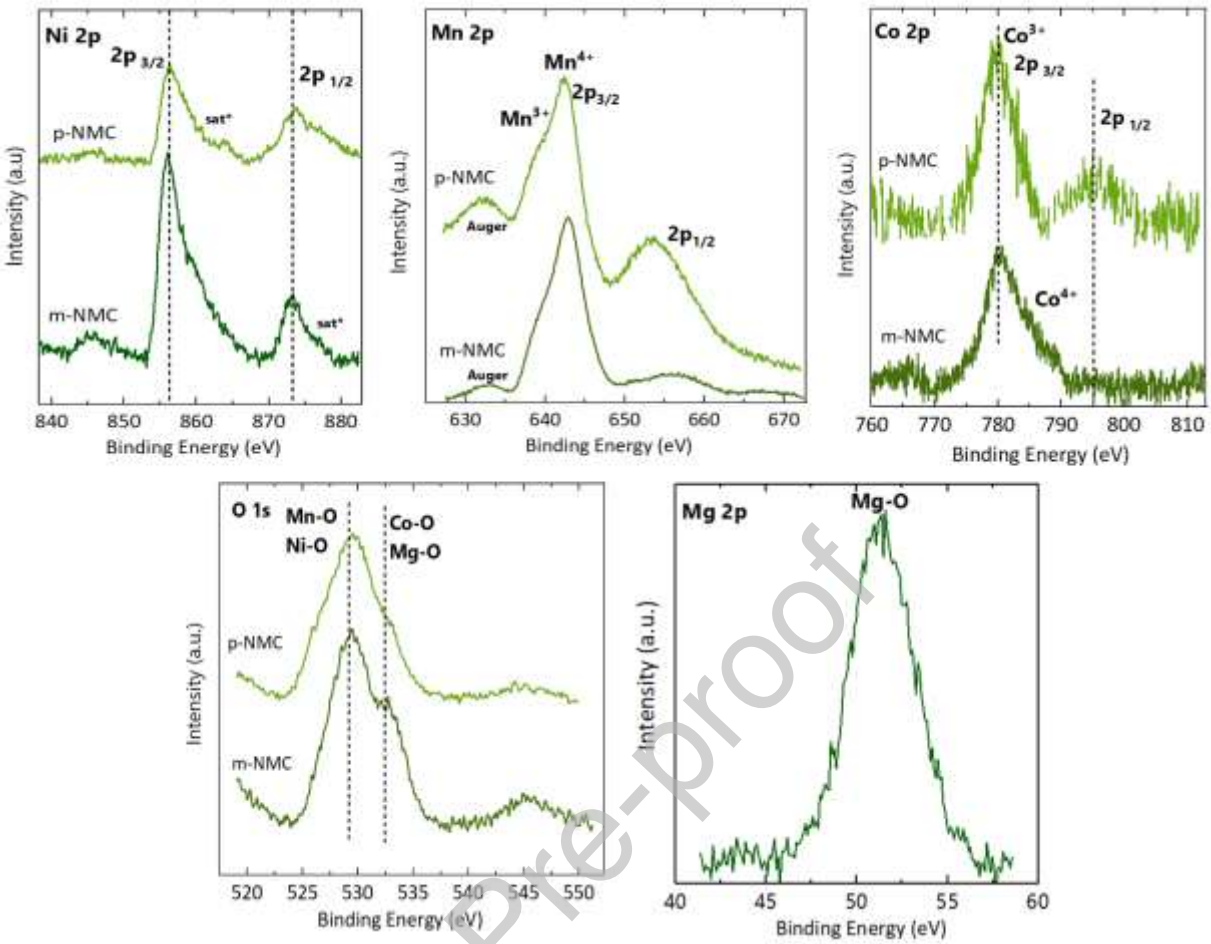

Figure 3. XPS spectra of p-NMC and m-NMC.

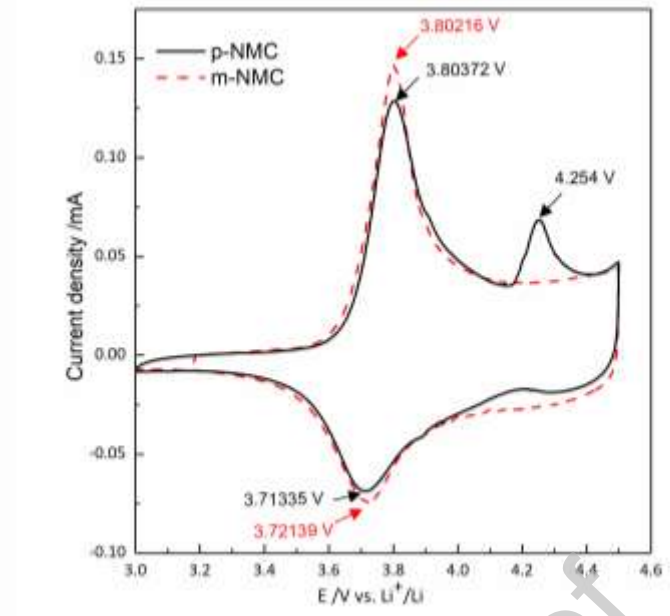

Figure 4. CV curves of p-NMC and m-NMC electrodes. Scan rate = 0.05 mVs^{-1}.

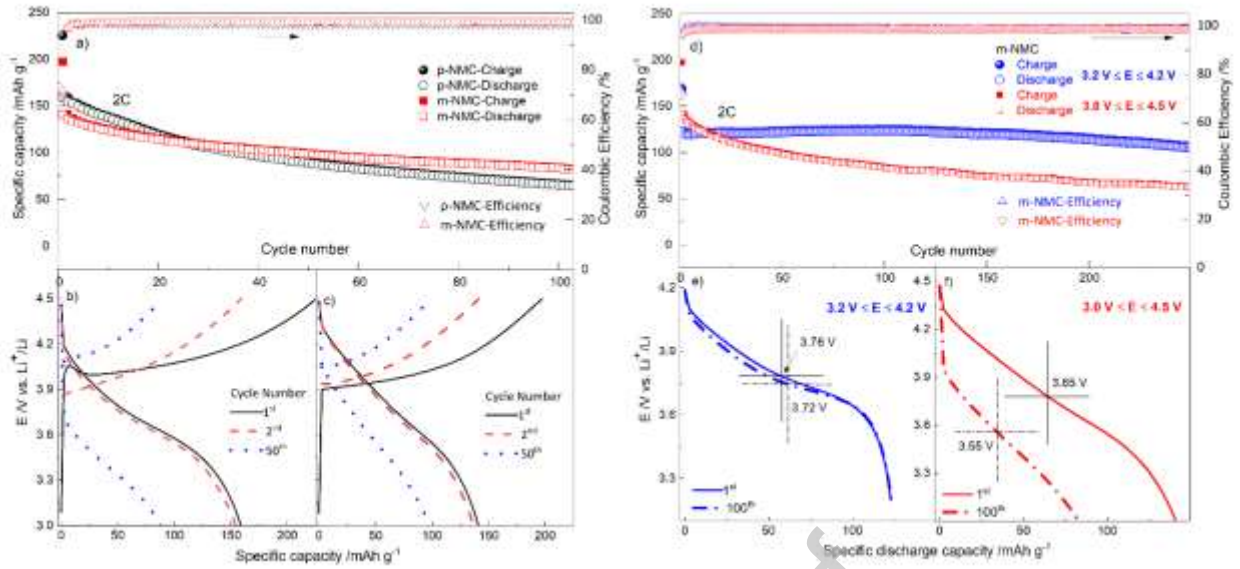

Figure 5. Charge/discharge capacity of p-NMC and m-NMC electrodes (a); charge/discharge profiles of selected cycles for p-NMC electrode (b), and m-NMC electrode (c). Charge/discharge capacity of m-NMC electrodes cycled in different potential windows (d); discharge profiles of 1st and 100th cycles for m-NMC electrode cycled in 3 V ≤ E ≤ 4.5 V range (e), for m-NMC electrode cycled in 3.2 V ≤ E ≤ 4.2 V range (c). I = 280 mA g^{-1}.

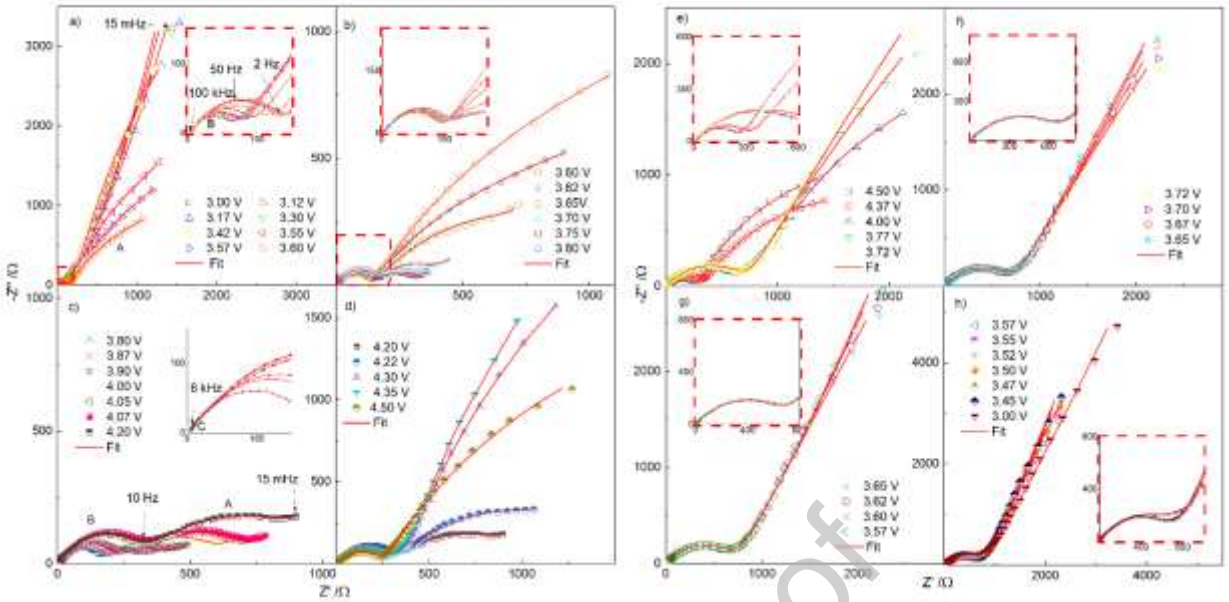

Figure 6. Nyquist plots recorded at selected potentials for p-NMC during the first oxidation (a-d) and during the first reduction (e-h).15 mHz < f < 100 kHz.

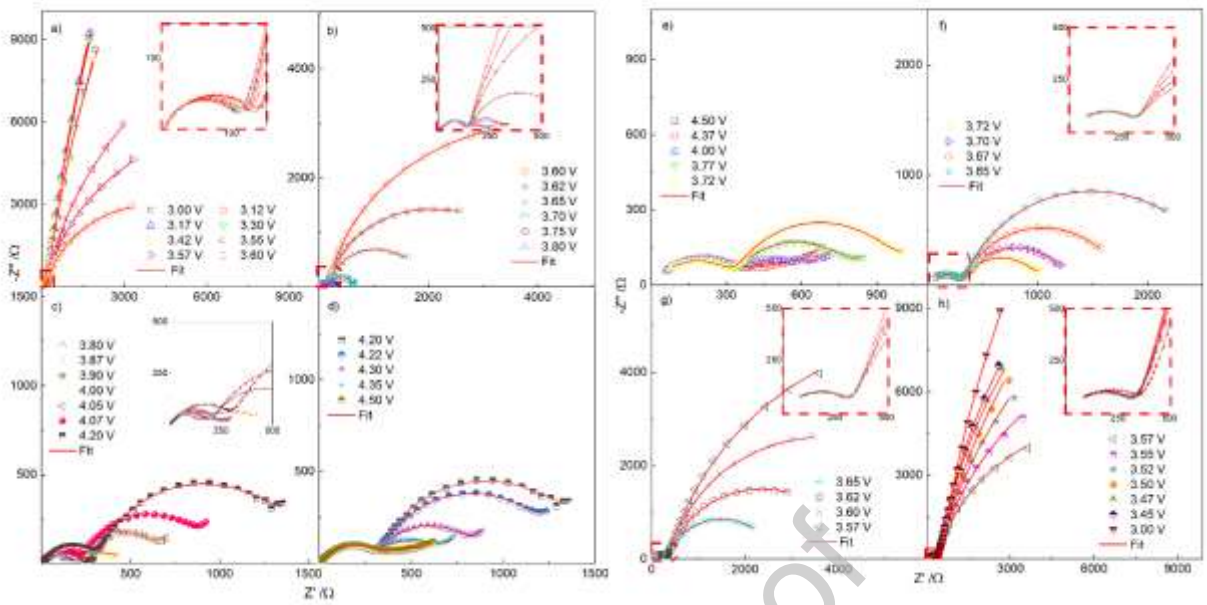

Figure 7. Nyquist plots recorded at selected potentials for m-NMC during the first oxidation (a-d) and during the first reduction (e-h).15 mHz < f < 100 kHz.

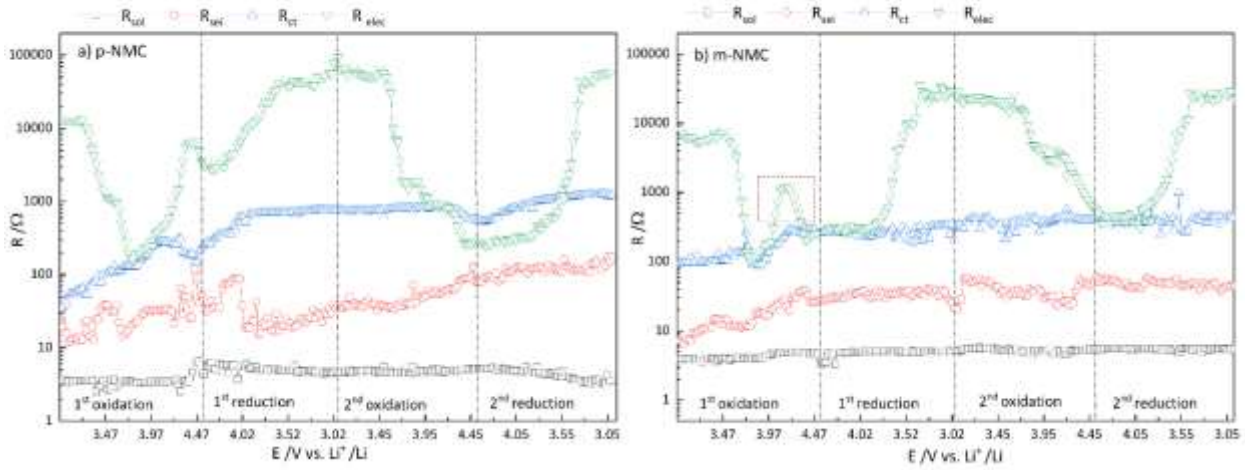

Figure 8. Fitted values of R_{sol}, R_{sei}, R_{ct}, R_{elec} during the first two cycles for (a) p-NMC and (b) m-NMC. 3 V ≤ E ≤ 4.5 V.

Table1: Rietveld refinement results for p-NMC and m-NMC materials.

Sample	Lattice parameter *a* /Å	Lattice parameter *c* /Å	c/a	$I_{(003)}/I_{(104)}$	$d_{(003)}$/Å	R_W (%)	R_P (%)
p-NMC	2.8587	14.2242	4.9757	1.45	4.7544	3.12	3.57
m-NMC	2.8691	14.2459	4.9652	1.53	4.7621	3.11	3.61